Xiaojue Zhu
Graduate Research Assistant
LNM, Institute of Mechanics,
Chinese Academy of Sciences,
Beijing 100190, China
e-mail: zhuxiaojue@lnm.imech.ac.cn

Guowei He
Professor and Director
LNM, Institute of Mechanics,
Chinese Academy of Sciences,
Beijing 100190, China
e-mail: hgw@lnm.imech.ac.cn

Xing Zhang[2]
Associate Professor
LNM, Institute of Mechanics,
Chinese Academy of Sciences,
Beijing 100190, China
e-mail: zhangx@lnm.imech.ac.cn

An Improved Direct-Forcing Immersed Boundary Method for Fluid-Structure Interaction Simulations[1]

In the present work, we present an improved version of the direct-forcing immersed boundary (IB) method proposed in Wang and Zhang (2011, "An Immersed Boundary Method Based on Discrete Stream Function Formulation for Two- and Three-Dimensional Incompressible Flows," J. Comput. Phys., ***230****(9), pp. 3479–3499). In order to obtain an accurate prediction of local surface force, measures have been taken to suppress the unphysical spatial oscillations in the Lagrangian forcing. A fluid-structure interaction (FSI) solver has been developed by using the improved IB method for the fluid and the finite difference method for the structure. Several flow problems are simulated to validate our method. The testing cases include flows over a stationary cylinder and a stationary flat plate, two-dimensional flow past an inextensible flexible filament, and three-dimensional flow past a flapping flag. The results obtained in the present work agree well with those from the literature.* [DOI: 10.1115/1.4026197]

1 Introduction

The phenomena of fluid-structure interaction are ubiquitous in nature such as flapping flags interacting with ambient fluid and swimming fish in water. The problems involving the coupled response of structures and flows are also of interest in various engineering areas such as aeronautical engineering, coastal engineering, and biomedical engineering. In such systems, the structures deform due to inertial, hydrodynamic, and internal forces; at the same time, they also exert forces on the surrounding fluid.

From a computational viewpoint, FSI simulations are challenging due to the following factors: (a) numerical issues (such as numerical instability) in handling two-way coupling between fluid and structure and (b) large mesh deformation when body-fitted mesh is used. The IB method overcomes the latter difficulty by using a nonbody-fitted mesh and adding a body force to the momentum equation to enforce the no-slip boundary condition [1]. The IB method can be further classified into two types: continuous-forcing and direct-forcing [2]. In the continuous-forcing approach, the forcing is incorporated into the continuous equations before discretization whereas in the direct-forcing approach, the forcing is introduced after the equations are discretized. The continuous-forcing approach is often used for treating elastic boundaries [1] whereas the direct-forcing approach is originally designed for rigid-boundary problems [3–5].

In this paper, we developed an FSI solver by coupling a direct-forcing IB method based on discrete stream function formulation [6] for the fluid and a finite different method for the structure. By using the original method proposed in Ref. [6], although an accurate prediction of total force and boundary condition can be achieved, unphysical spatial oscillation is observed in the force distribution. This oscillation is detrimental to the prediction of structure response in FSI. In this work, several modifications are made to improve this method. Firstly, the implicit forcing [6,7] is replaced by an explicit forcing [8]. It is found that the use of implicit forcing by solving a linear system can lead to severe oscillation in Lagrangian force, but explicit forcing would not. Secondly, a more consistent way for computing each component of the forcing on a staggered mesh is proposed. In the original method, the Eulerian force *vector* is defined at the cell center; each velocity *component* (which is defined at the edge center) is obtained by interpolation if needed. Now the Eulerian force vector is not used, and we only need to define the Eulerian force component at edge center. Thirdly, the Lagrangian grid width is set to be twice that of the Eulerian grid; such a setting can result in smoother Lagrangian force distribution. Fourthly, for a slender body of zero thickness, the discrete δ-function with a "negative-tail" is adopted for the interpolations at the endpoints. Numerical simulations (including FSI) are performed to test the efficacy of these modifications. It is found that the measures taken can successfully reduce the oscillations, and the results obtained agree well with those from the literature.

The rest of the paper is arranged as follows. The numerical method is briefly introduced in Sec. 2. The testing cases, including flows over a stationary cylinder and a flat plate, flows past a flexible filament, and a flag are presented in Sec. 3. Finally, conclusions are drawn in Sec. 4.

2 Numerical Methods

2.1 Governing Equations. The fluid motion is governed by the incompressible Navier–Stokes (N–S) equations, which in dimensionless form are written as

$$\frac{\partial \mathbf{u}}{\partial t} + \nabla \cdot (\mathbf{u}\mathbf{u}) = -\nabla p + \frac{1}{\mathrm{Re}}\nabla^2 \mathbf{u} + \mathbf{f} \tag{1}$$

$$\nabla \cdot \mathbf{u} = 0 \tag{2}$$

where $\mathbf{u}$ is the velocity vector, p is the pressure, and Re is the Reynolds number. $\mathbf{f}$ is the Eulerian body-force that is used to mimic the effects of the immersed body on the flow. The Reynolds number is defined as

[1] This manuscript is submitted to the special issue on immersed boundary method. Preliminary version of this paper appeared as FEDSM2013-16472 in ASME 2013 Fluids Engineering Division Summer Meeting, Incline Village, NV, July 7–11, 2013.

[2] Corresponding author.

Contributed by the Fluids Engineering Division of ASME for publication in the Journal of Fluids Engineering. Manuscript received May 13, 2013; final manuscript received December 4, 2013; published online February 28, 2014. Assoc. Editor: Zhongquan Charlie Zheng.

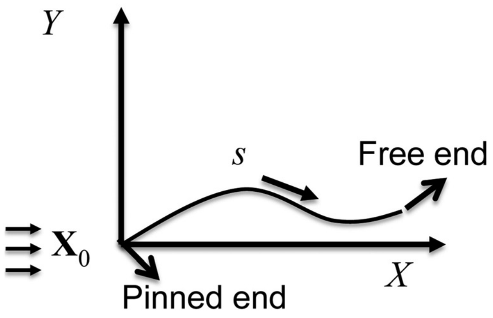

Fig. 1 Schematic representation of the Lagrangian coordinate system *s* on the filament. The length of the filament is *L*.

$$\mathrm{Re} = \frac{UL}{\nu} \tag{3}$$

where U, L, and ν are the reference length, reference velocity, and kinematic viscosity, respectively. In our simulations, U equals the inflow velocity, and L is the diameter of the cylinder or the length of a filament (flag).

In this paper, two FSI simulations are performed. The first case is the interaction of an inextensible flexible filament with a two-dimensional flow. The flexible filament can be regarded as a one-dimensional flag. The governing equations for the motion of the filament are

$$\beta\frac{\partial^2\mathbf{X}}{\partial t^2} - \frac{\partial}{\partial s}\left(T\frac{\partial\mathbf{X}}{\partial s}\right) + \frac{\partial^2}{\partial s^2}\left(\gamma\frac{\partial^2\mathbf{X}}{\partial s^2}\right) = \beta Fr\frac{\mathbf{g}}{g} - \mathbf{F} \tag{4}$$

$$\frac{\partial\mathbf{X}}{\partial s}\cdot\frac{\partial\mathbf{X}}{\partial s} = 1 \tag{5}$$

where s is the Lagrangian coordinate along the arc length, $\mathbf{X}$ is the displacement vector, and β, T, and γ are the mass ratio, dimensionless tension coefficient, and dimensionless bending rigidity, respectively. $\mathbf{F}$ is the Lagrangian force, and $\mathbf{g}$ is the acceleration of gravity and $g = |\mathbf{g}|$. Fr is the Froude number. Equation (4) is equivalent to those used by Zhu and Peskin [9], Connell and Yue [10], and Huang et al. [11] for flexible structures. Equation (5) is the inextensible condition. Figure 1 shows the Lagrangian coordinates used in the simulation of a flapping filament.

The boundary condition at the free end is

$$T = 0, \quad \frac{\partial^2\mathbf{X}}{\partial s^2} = (0,0), \quad \frac{\partial^3\mathbf{X}}{\partial s^3} = (0,0) \tag{6}$$

At the fixed end, the simply supported boundary condition is applied.

$$\mathbf{X} = \mathbf{X}_0, \quad \frac{\partial^2\mathbf{X}}{\partial s^2} = (0,0) \tag{7}$$

The second case of FSI is the interaction of a flag (flexible plate) with a three-dimensional flow. The governing equations of the motion of the flag are written as

$$\beta\frac{\partial\mathbf{X}}{\partial t^2} = \sum_{i,j=1}^{2}\left[\frac{\partial}{\partial s_i}\left(\sigma_{ij}\frac{\partial\mathbf{X}}{\partial s_j}\right) - \frac{\partial^2}{\partial s_i\partial s_j}\left(\gamma_{ij}\frac{\partial^2\mathbf{X}}{\partial s_i\partial s_j}\right)\right] + \beta Fr\frac{\mathbf{g}}{g} - \mathbf{F} \tag{8}$$

$$\sigma_{ij} = \varphi_{ij}\left(\frac{\partial\mathbf{X}}{\partial s_i}\cdot\frac{\partial\mathbf{X}}{\partial s_j} - \delta_{ij}\right) \tag{9}$$

where φ_{ij} $(i,j = 1$ or $2)$ are the stretching and shearing coefficients, σ_{ij} $(i,j = 1$ or $2)$ are the stretching and shearing forces, and γ_{ij} $(i,j = 1$ or $2)$ are the bending and twisting coefficients. δ_{ij} is the Kronecker symbol. When $i = j$, $\delta_{ij} = 1$, and when $i \neq j$, $\delta_{ij} = 0$. In this study, we consider an inextensible flag by making the stretching coefficients φ_{11} and φ_{22} sufficiently large. Equations (8) and (9) are equivalent to those used by Huang and Sung [12]. Figure 2 shows the Lagrangian coordinates used in the simulation of a flapping flag.

At the fixed end, we consider the simply supported condition in the simulation, i.e.,

$$\mathbf{X} = (0,0,s_2), \quad \frac{\partial^2\mathbf{X}}{\partial s_1^2} = 0 \quad \text{at} \quad s_1 = 0 \tag{10}$$

At the free boundaries, the boundary conditions are

$$\frac{\partial^2\mathbf{X}}{\partial s_1^2} = 0, \quad \frac{\partial^3\mathbf{X}}{\partial s_1^3} = 0 \quad \text{at} \quad s_1 = L \tag{11}$$

$$\frac{\partial^2\mathbf{X}}{\partial s_2^2} = 0, \quad \frac{\partial^3\mathbf{X}}{\partial s_2^3} = 0 \quad \text{at} \quad s_1 = 0 \text{ or } H \tag{12}$$

and

$$\sigma_{ij} = 0, \quad \gamma_{ij} = 0 \ (i,j = 1,2) \tag{13}$$

2.2 Direct-Forcing IB Method Based on Discrete Stream Function Formulation. We use the discrete stream function approach for solving the Navier–Stokes equations. For more details of this approach, please refer to Ref. [6]. The discretized form of Eqs. (1) and (2) can be expressed by a matrix form as

$$\begin{bmatrix}\mathbf{A} & \mathbf{G}\\ \mathbf{D} & 0\end{bmatrix}\begin{bmatrix}q^{n+1}\\ p\end{bmatrix} = \begin{bmatrix}r^n\\ 0\end{bmatrix} + \begin{bmatrix}bc_1\\ bc_2\end{bmatrix} + \begin{bmatrix}f\\ 0\end{bmatrix} \tag{14}$$

where q, p, and f are the discrete velocity flux, pressure, and body force, respectively. q is related to the discrete velocity u by multiplying the cell face area. $\mathbf{A}$, $\mathbf{G}$, and $\mathbf{D}$ are the implicit operator, gradient operator, and divergence operator, respectively. r^n is the explicit right-hand side term of the momentum equation. bc_1 and bc_2 are the boundary condition vectors for the momentum and continuity equations, respectively.

In the discrete stream function approach, a discrete streamfunction $\tilde{s}$ is defined as

$$q = \mathbf{C}\tilde{s} \tag{15}$$

where $\mathbf{C}$ is the curl operator. This matrix is constructed in such a way that $\mathbf{D}$ and $\mathbf{C}$ enjoy the following relation:

$$\mathbf{DC} = \mathbf{0} \tag{16}$$

The definition in Eq. (15), together with the relation in Eq. (16), guarantees the discrete incompressibility. In the discrete stream function approach, another type of curl operator, the rotational operator $\mathbf{R}$, is also defined such that matrix $\mathbf{R}$ and matrix $\mathbf{C}$ enjoy the following relation:

$$\mathbf{R} = \mathbf{C}^T \tag{17}$$

By premultiplying the momentum equation with $\mathbf{R}$, the pressure can be eliminated from the system. This can be easily seen in the identity equation

$$\mathbf{RG} = -\mathbf{C}^T\mathbf{D}^T = -(\mathbf{DC})^T = \mathbf{0} \tag{18}$$

Thus, the system of Eq. (14) is reduced to a single equation for $\tilde{s}$ at each time step

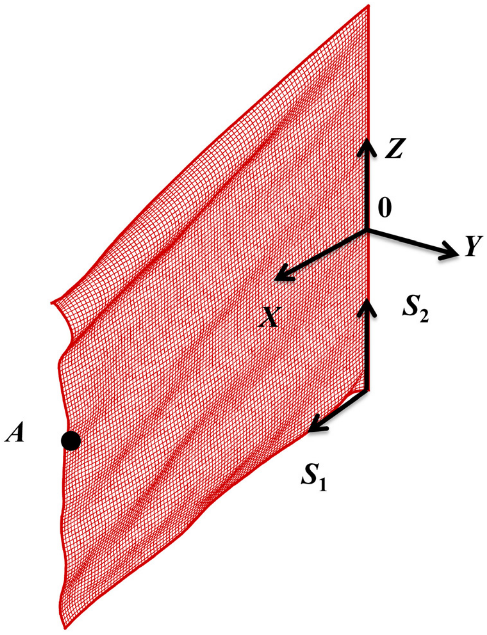

Fig. 2 Schematic representation of the Lagrangian coordinate system s_1 and s_2 on the flag. The longitudinal coordinate s_1 ranges from 0 to L, and the spanwise coordinate s_2 ranges from 0 to H, where L and H denote the length and width of the flag, respectively.

$$\mathbf{C}^T\mathbf{AC}\tilde{s}^{n+1} = \mathbf{R}(r^n - bc_1) + \mathbf{R}f = \mathbf{R}r'^n + \mathbf{R}f \qquad (19)$$

The representations of these operators are given in Ref. [6]. As to the time advancement, the diffusion term is implicit, the convection term is treated explicitly, and a three-step, second-order, low storage, Runge–Kutta scheme is used [6].

The matrix $\mathbf{C}^T\mathbf{AC}$ is symmetric, positive-definite, and thus can be solved using the conjugate gradient (CG) method. A brief introduction of this iterative method, including the preconditioner and convergence criterion, is given in Ref. [6]. After solving Eq. (19), the velocity components can be recovered through Eq. (15). Although pressure is eliminated in this approach, if it is required, it can still be obtained through a postprocessing step, which is independent of the solution procedure for the velocity field.

The flow solver is based on the direct-forcing IB method in discrete stream function formulation. The original IB method in Ref. [6] can be summarized as follows:

$$\mathbf{RAC}\tilde{s}^* = \mathbf{R}r'^n + \mathbf{R}f^n \qquad (20)$$

$$\vec{u}^* = \mathbf{C}\tilde{s}^* \qquad (21)$$

$$\vec{U}^*(\mathbf{X}_k) = \sum_x \vec{u}^*(\mathbf{x})\delta_h(\mathbf{x} - \mathbf{X}_k)h^3 \qquad (22)$$

$$\sum_{j=1}^{M}\left(\sum_x \delta_h(\mathbf{x} - \mathbf{X}_k)\delta_h(\mathbf{x} - \mathbf{X}_j)\Delta s h^3\right)\vec{F}'(\mathbf{X}_j) = \frac{\vec{U}^d(\mathbf{X}_k) - \vec{U}^*(\mathbf{X}_k)}{\Delta t} \qquad (23)$$

$$F^{n+1} = F^n + F' \qquad (24)$$

$$f^{n+1}(\mathbf{x}) = \sum_{j=1}^{M} F^{n+1}(\mathbf{X}_j)\delta_h(\mathbf{x} - \mathbf{X}_j)\Delta s \qquad (25)$$

$$\mathbf{RAC}\tilde{s}^{n+1} = \mathbf{R}r'^n + \mathbf{R}f^{n+1} \qquad (26)$$

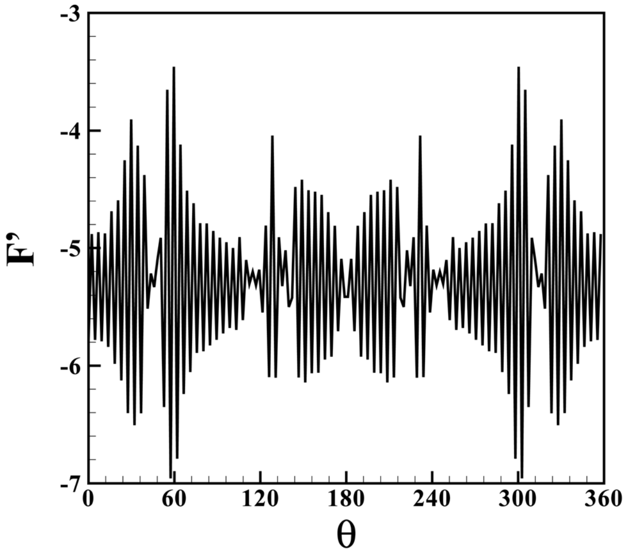

Fig. 3 The distribution of Lagrangian force correction F'_x along the cylinder's surface by using Eq. (23) and setting the right hand side of Eq. (23) to −100 at each Lagrangian point. The Lagrangian grid width and Eulerian grid width are both 0.02. θ denotes the angle between the radical direction and the horizontal direction.

$$\vec{u}^{n+1} = \mathbf{C}\tilde{s}^{n+1} \qquad (27)$$

Here h and Δs are Eulerian and Lagrangian grid size, respectively. By introducing the discrete stream-function in Eq. (20) and Eq. (26), the pressure term is eliminated and the divergence-free condition can be satisfied to machine precision [6]. The direct-forcing procedure of the IB method is described as follows. First, a "predicted" (tentative) velocity $\vec{u}^*$ is computed by using the force components of the previous time step n (Eqs. (20) and (21)). In the next step (Eq. (22)), $\vec{u}^*$ is interpolated to the boundary. The Lagrangian force correction F' is then determined by solving a small linear system (Eq. (23)). Subsequently, F^{n+1} is updated by Eq. (24) and then spread to the grid points near the boundary by Eq. (25). Finally, the velocity $\vec{u}^{n+1}$ is computed with the updated forcing term f^{n+1} by Eqs. (26) and (27).

The regularized Delta function used in the present study is defined as

$$\delta_h(\mathbf{x} - \mathbf{X}) = \frac{1}{h^3}\phi\left(\frac{x-X}{h}\right)\phi\left(\frac{y-Y}{h}\right)\phi\left(\frac{z-Z}{h}\right) \qquad (28)$$

Here ϕ is in the form of a four-point piecewise δ function that is proposed in [1]

$$\phi(r) = \begin{cases} \frac{1}{8}\left(3 - 2|r| + \sqrt{1 + 4|r| - 4r^2}\right), & |r| \le 1 \\ \frac{1}{8}\left(5 - 2|r| - \sqrt{-7 + 12|r| - 4r^2}\right), & 1 \le |r| \le 2 \\ 0, 2 \le |r| \end{cases} \qquad (29)$$

Although an accurate prediction of total force can be achieved by using this method, unphysical spatial oscillation is observed in the Lagrangian force distribution on the surface of the immersed body. This oscillation is due to the "implicit" treatment of Lagrangian force in Eq. (23) and error accumulation in every time step in Eq. (24). Since the Lagrangian force oscillation is detrimental to the prediction of structure response in FSI, several modifications are made in the present work to improve this method.

Firstly, it is found that even if the right-hand side is smooth, oscillation still exists in the Lagrangian force distribution by using

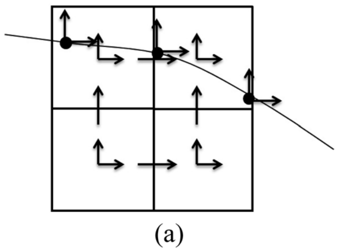
(a)

(b)

Fig. 4 Two ways of computing forcing component on a staggered mesh: (*a*) original way used in Ref. [6] and (*b*) more consistent way of computing forcing component. In (*a*), the Eulerian forcing (vector) is defined at cell centers, and each forcing component is interpolated (individually) to cell edges via simple average. In (*b*), each Eulerian forcing component is defined at cell edges, and no extra interpolation is needed.

Table 1 Influence of the ratio of Lagrangian grid width to Eulerian grid width on drag coefficients and oscillation in $\vec{U}^*$ by using the four-point delta function in the simulation of flow over a cylinder at Re = 40. N_L is the number of Lagrangian grid points.

$\Delta s/h$	N_L	C_d	Oscillations in $\vec{U}^*$
2.5	63	1.56	No
2	79	1.56	No
1.5	105	1.56	Yes
1	157	1.56	Yes

Eq. (23) (see Fig. 3). Thus, the implicit forcing in Eq. (23) is replaced by the explicit forcing proposed by Uhlmann [8] (Eq. (30)). The explicit direct-forcing can be written as

$$\frac{\vec{F}'(\mathbf{X}_j)}{\Delta s} = \frac{\vec{U}^d(\mathbf{X}_k) - \vec{U}^*(\mathbf{X}_k)}{\Delta t} \tag{30}$$

Secondly, a more consistent way of computing the momentum forcing on a staggered mesh is proposed (see Fig. 4). Instead of obtaining the forcing vectors at cell centers and then averaging them to edge centers to obtain individual components, the x- and y-components of the forcing vectors are computed separately and directly at edge centers. It is believed that the averaging operations on a nonsmooth function (such as velocity) tends to reduce accuracy.

Thirdly, the ratio between the Lagrangian grid width Δs and Eulerian grid width h is set at 2. Table 1 shows the influences of $\Delta s/h$ on drag coefficient of a circular cylinder using the four-point δ function at Re $= 40$. No difference in drag coefficient is seen by using various $\Delta s/h$. It is also seen that by increasing $\Delta s/h$ to 2 or even larger, no oscillation in Lagrangian force distribution is observed. As shown in Fig. 5, $\vec{U}^*$ exhibits spatial oscillation at $\Delta s/h = 1$ while no oscillation is observed at $\Delta s/h = 2$. Thus, in all the validation cases of this work, $\Delta s/h$ is set to 2. It is believed that this type of oscillation is due to the accumulation of velocity errors in the temporal advancement.

Fourthly, for a slender body of zero-thickness, the discrete δ-function with a "negative-tail" is adopted for the interpolation at endpoints. The mathematical form of this δ function [13] is

$$\phi(r) = \begin{cases} 1-(1/2)|r|-|r|^2+(1/2)|r|^3, & |r|\le 1.0 \\ 1-(11/6)|r|+|r|^2-(1/6)|r|^3, & 1.0\le|r|\le 2.0 \\ 0, & |r|\ge 2.0 \end{cases} \tag{31}$$

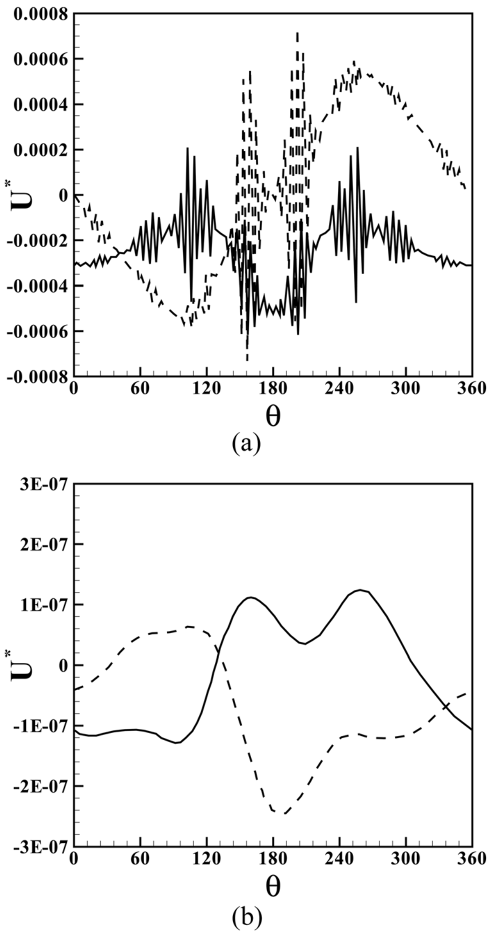

(a)

(b)

Fig. 5 The distribution of Lagrangian intermediate velocity $\vec{U}^*$ along the cylinder's surface. The Eulerian grid width is 0.02 while in case (*a*) $\Delta s/h = 1$ and in case (*b*) $\Delta s/h = 2$.

It is found that the strong (unphysical) backflow at the leading- and trailing-edge of the zero-thickness plate is another source of spatial oscillation. The use of this type of kernel function can effectively eliminate the backflow at the endpoints. For the rest of the Lagrangian points (other than the endpoints), the regular four-point δ function (Eq. (29)) is used.

2.3 Discretization of the Structural Equations for Flexible Filament and Flag.

The first case is a flexible filament. A finite difference method on staggered grid [11] is used to discretize Eq. (4) and Eq. (5). The displacement $\mathbf{X}$ is defined at grid nodes while the tension T is defined at the centroids of grid cells. Let D_s denote the central difference operator with respect to s, for an arbitrary variable ψ, $D_s\psi$ means

$$D_s\psi = (\psi(s+\Delta s/2) - \psi(s-\Delta s/2))/\Delta s \tag{32}$$

$\mathbf{F}_b$ denotes the bending force (i.e., the second term on the right-hand side of Eq. (4)). The solution procedure can be summarized as follows:

$$\mathbf{X}^* = 2\mathbf{X}^n - \mathbf{X}^{n-1} \tag{33}$$

$$\begin{aligned}&(D_s(D_s(T^{n+\frac{1}{2}}D_s\mathbf{X}^*)))_{k+\frac{1}{2}}\cdot(D_s\mathbf{X}^*)_{k+\frac{1}{2}}\\ &= \beta\frac{1-2(D_s\mathbf{X}\cdot D_s\mathbf{X})^n+(D_s\mathbf{X}\cdot D_s\mathbf{X})^{n-1}}{2\Delta t^2} - \\ &\beta(D_s\mathbf{U}\cdot D_s\mathbf{U})^n_{k+\frac{1}{2}} - (D_s\mathbf{X}^*)_{k+\frac{1}{2}}\cdot(D_s(\mathbf{F}_b^n-\mathbf{F}^n))_{k+\frac{1}{2}}\end{aligned} \tag{34}$$

$$\beta\frac{\mathbf{X}_k^{n+1}-\mathbf{X}_k^*}{\Delta t^2} = (D_s(T^{n+\frac{1}{2}}D_s\mathbf{X}^{n+1}))_k + (\mathbf{F}_b)_k^n - \mathbf{F}_k^n + \beta Fr\frac{\mathbf{g}}{g} \tag{35}$$

Table 2 Comparisons of lift and drag coefficients, Strouhal numbers for flows over a cylinder at different Reynolds numbers

Case	Re	C_d	C_l	St
Present	40	1.55	±0.00	–
Linnick and Fasel [14]	40	1.54	±0.00	–
Taira and Colonius [15]	40	1.54	±0.00	–
Wang and Zhang [6]	40	1.54	±0.00	–
Present	100	1.35	±0.33	0.166
Linnick and Fasel [14]	100	1.38	±0.33	0.169
Uhlmann [8]	100	1.45	±0.34	0.169
Wang and Zhang [6]	100	1.33	±0.32	0.166
Present	200	1.34	±0.69	0.197
Linnick and Fasel [14]	200	1.34	±0.69	0.197
Taira and Colonius [15]	200	1.35	±0.68	0.196
Wang and Zhang [6]	200	1.32	±0.69	0.197

Equation (34) is the discretized form of the Poisson equation, which can be derived from Eq. (4) and the inextensibility condition Eq. (5) [11]. With the boundary condition in Eq. (6) and Eq. (7), the filament's motion can be solved directly by using the CG method.

The second case is a flapping flag. A finite difference method is used to discretize Eqs. (8) and (9). We use a uniform mesh with mesh width Δs in both s_1 and s_2 directions. For an arbitrary variable ψ, the first-order central differences of ψ along s_1 and s_2 are

$$(D_1\psi)_{i+\frac{1}{2},j} = \frac{\psi_{i+1,j} - \psi_{i,j}}{\Delta s} \tag{36}$$

$$(D_2\psi)_{i,j+\frac{1}{2}} = \frac{\psi_{i,j+1} - \psi_{i,j}}{\Delta s} \tag{37}$$

The second-order central difference and cross difference are expressed as

$$(D_{11}\psi)_{i,j} = \frac{(D_1\psi)_{i+\frac{1}{2},j} - (D_1\psi)_{i-\frac{1}{2},j}}{\Delta s} \tag{38}$$

$$(D_{22}\psi)_{i,j} = \frac{(D_2\psi)_{i,j+\frac{1}{2}} - (D_2\psi)_{i,j-\frac{1}{2}}}{\Delta s} \tag{39}$$

$$(D_{12}\psi)_{i+\frac{1}{2},j+\frac{1}{2}} = \frac{(D_2\psi)_{i+1,j+\frac{1}{2}} - (D_2\psi)_{i,j+\frac{1}{2}}}{\Delta s} \tag{40}$$

$$(D_{21}\psi)_{i+\frac{1}{2},j+\frac{1}{2}} = \frac{(D_1\psi)_{i+\frac{1}{2},j+1} - (D_1\psi)_{i+\frac{1}{2},j}}{\Delta s} \tag{41}$$

where D_{11} and D_{22} denote the second-order difference along the s_1 and s_2 direction. D_{12} and D_{21} are cross differences.

Using the definitions above, the discretized form of the flag's equations (Eqs. (8) and (9)) can be written as

$$\sigma_{ij} = \varphi_{ij}(D_i\mathbf{X}\cdot D_j\mathbf{X} - \delta_{ij}) \tag{42}$$

$$\beta\frac{\mathbf{X}^{n+1} - 2\mathbf{X}^n + \mathbf{X}^{n-1}}{\Delta t} = \sum_{i,j=1}^{2}[D_i(\sigma_{ij}D_j\mathbf{X}) - D_{ij}(\gamma_{ij}D_{ij}\mathbf{X})]^{n+1} - \mathbf{F}^n \tag{43}$$

Together with the boundary conditions (Eqs. (10)–(13)), the flag's motion can be solved by using the CG method.

For the coupling of the fluid and structure, we use a staggered (or loosely-coupled) method, in which the flow solver and structure solver are alternatively advanced by one step in time. In the framework of the direct-forcing IB method, the velocity of the filament obtained in the structural solver provides the boundary condition for the fluid solver, i.e., $\mathbf{U}^d = \dot{\mathbf{X}}$, while the Lagrangian force $\mathbf{F}$ determined in the flow solver acts as the source term in the structural equation.

Table 3 Grid refinement results and convergence order obtained by using flow past a cylinder at Re = 40

h/D	$\varepsilon_\infty^{(h)}$	$\varepsilon_\infty^{(2h)}/\varepsilon_\infty^{(h)}$	O_∞	$\varepsilon_2^{(h)}$	$\varepsilon_2^{(2h)}/\varepsilon_2^{(h)}$	O_2
1/16	1.04e-1	–	–	7.24e-2	–	–
1/32	3.50e-2	2.97	1.57	2.36e-2	3.07	1.62
1/64	1.21e-2	2.91	1.54	7.89e-3	2.99	1.58
1/128	4.19e-3	2.87	1.52	2.65e-3	2.95	1.56
1/256	1.28e-3	3.32	1.73	8.20e-4	3.25	1.70

3 Numerical Validations and Results

3.1 Flows Over a Cylinder. To validate the solver, first the numerical study of flow over a stationary cylinder at $\mathrm{Re} = 40, 100, 200$ is conducted. The simulation is performed in a rectangular domain of $30D \times 40D$, where D is the diameter of the cylinder. The cylinder is placed on the centerline with its center being $10D$ away from the inlet. The grid size in the vicinity of the cylinder (a region of $2D \times 2D$) is $0.02D$. The grids are stretched to the boundaries with an expansion factor of 1.05, and the maximum grid size is $0.2D$. The Lagrangian points are evenly distributed along the circumference of the circular cylinder and $\Delta s/h = 2.0$. The time step is chosen such that the Courant–Friedrichs–Lewy (CFL) number never exceeds 0.5.

First, we compute lift and drag by the summation of the two components of the Lagrangian forcing, respectively. As that listed in Table 2, the lift and drag coefficients obtained in the present study agree well with those from the references.

A refinement study is also performed employing the improved IB method to assess its convergence behavior. We choose the flow over a stationary cylinder at $\mathrm{Re} = 40$ as a benchmark problem. We use uniform grids in this test and the computational domain is the same as that aforementioned. Spatial and temporal step sizes are reduced simultaneously by fixing the CFL number to 0.5 in all cases. The Lagrangian points are evenly distributed along the circumference of the circular cylinder and $\Delta s/h = 2.0$. Since there is no analytical solution for this problem, the numerical results are compared to the reference solution obtained on a very fine grid with the grid width of $(1/512)D$ (where D is the diameter of the cylinder). Thus, the L_∞ -error and L_2 -error can be defined as

$$\varepsilon_\infty = \max\{u_{i,j} - u_{i,j}^{\mathrm{ref}}\} \tag{44}$$

$$\varepsilon_2 = \sqrt{\frac{\sum_{i=1}^{N_x}\sum_{i=1}^{N_y}(u_{i,j} - u_{i,j}^{\mathrm{ref}})^2}{N_xN_y}} \tag{45}$$

The order of convergence O is computed by using different errors obtained on successively refined grids, i.e.,

$$O = \frac{\log(\varepsilon^{(2h)}/\varepsilon^{(h)})}{\log 2} \tag{46}$$

Table 3 shows that the convergence order of this method is between 1 and 2 (around 1.55). This is consistent with the results for many variants of IB methods, which use a second-order accurate basic N–S solver.

Next, we compute the pressure and skin-friction for the case of Re = 40 by projecting the Lagrangian forcing on the local normal and tangential direction, respectively. The distributions of the

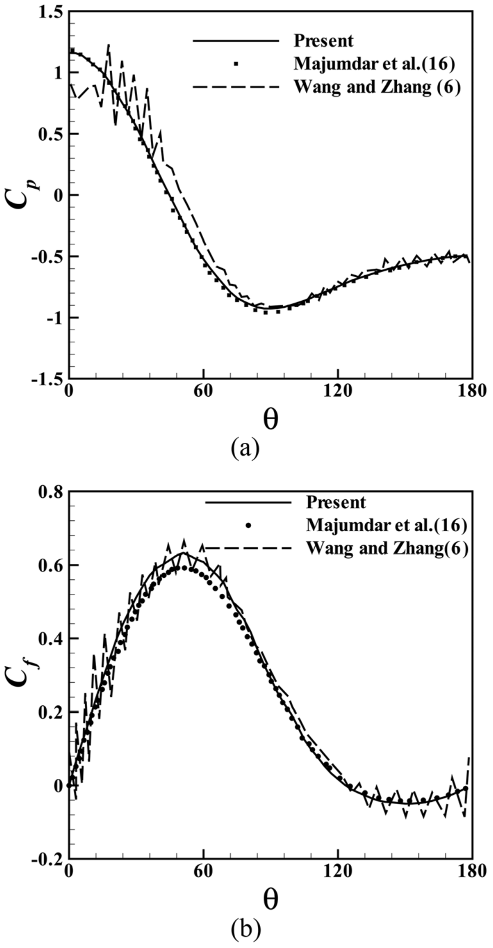

Fig. 6 Distribution of (*a*) pressure coefficient C_p and (*b*) skin-friction coefficient C_f on the surface of the cylinder for Re = 40

pressure coefficient C_p and skin-friction coefficient C_f obtained by using the improved method are compared with the reference solutions in Ref. [16] and the solution by using the original method proposed in Ref. [6] (see Fig. 6). It is seen that a good agreement between the present result and the reference solution in Ref. [16] has been achieved. From this figure, it is also seen that the result obtained by using the method in Ref. [6] exhibits large spatial oscillations in both pressure and skin-friction.

3.2 Flows Over a Flat Plate.

We then simulate the flow over a flat plate at $\mathrm{Re} = 200$ and two angles of attack (0 deg and 10 deg). The purpose of this validation is to test the accuracy of force distribution prediction for a slender body of zero-thickness. In this simulation, we use a rectangular domain of $30L \times 20L$. The flat-plate is placed on the centerline with its center being $10L$ away from the inlet. The grid size in the vicinity of the plate (a region of $2L \times 2L$) is $0.01L$. The time step is chosen such that the CFL number never exceeds 0.5. For reference purpose, we seek the solution of this problem by using the commercial computational fluid dynamics software-FLUENT. A body-fitted unstructured mesh with 140,000 cells is used in the computation by FLUENT. The mesh resolution used in FLUENT is comparable to that in the in-house flow solver (with the thickness of the plate represented by three mesh points in FLUENT). Other numerical settings in FLUENT are: second-order upwind scheme for convection, second-order central scheme for diffusion, and first-order Euler scheme for time advancing.

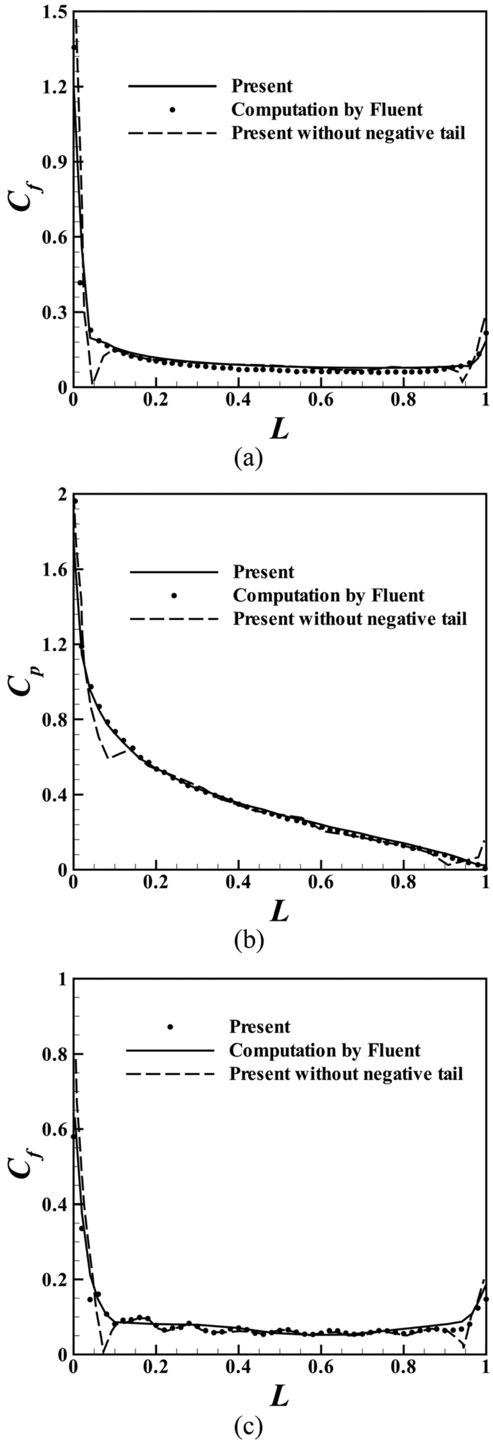

Fig. 7 Distributions of pressure coefficient difference ΔC_p and skin-friction coefficient (C_f) along the flat-plate surface at Re = 200 and two angles of attack: (*a*) C_f for $\alpha = 0$ deg, (*b*) ΔC_p for $\alpha = 10$ deg, and (*c*) C_f for $\alpha = 10$ deg

The distributions of pressure (difference) and skin-friction, obtained by using the improved method, by using the improved method but without the "negative-tailed" δ function and by using FLUENT, are plotted in Fig. 7. It is seen that the agreement between the result obtained using the improved method and the one using FLUENT is reasonably well. The result using the improved method but without the "negative-tailed" δ function exhibits some oscillations near the leading- and trailing-edge of the flat plate.

3.3 Flapping of Flexible Filament.

Before performing any FSI simulation, we first validate the stand-alone structure solver

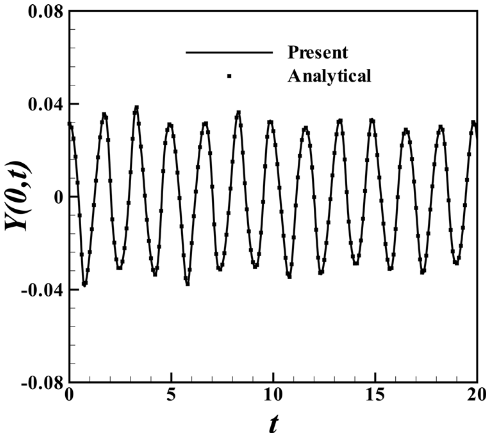

Fig. 8 Comparison of the predicted free-end position with the analytical result

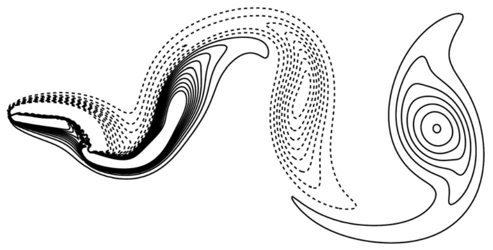

Fig. 9 Vorticity contours in wake of a flapping flexible filament

by simulating a flexible filament moving under gravity in vacuum. The simply supported (pinned) boundary condition is used at one end, and the free-end boundary condition is used at the other (see Fig. 1). The initial position condition of the filament is given by $\mathbf{X}(s,0) = \mathbf{X}_0 + (L-s)(\cos k, \sin k)$, $\partial \mathbf{X}(s,0)/\partial t = (0,0)$, where k is a constant and $\mathbf{X}_0 = (0,0)$. At $t = 0$, the filament is released and starts swinging due to the gravitational force.

We use $\beta = 1.0$, $L = 1.0$, $Fr = 10.0$, $\gamma = 0$, and $k = 0.1\pi$ as the control parameters. As shown in Fig. 8, the numerically predicted free-end position agrees well with the analytical solution in Ref.[11].

We then simulate the interaction of a flexible filament with a free stream at $\mathrm{Re} = 200$. We use a computational domain of $16L \times 10L$. The distance between the leading edge of the filament and the inlet is $6L$. The mesh size is $0.01L$ in the vicinity of the filament (a region of $6L \times 2L$). The number of the Lagrangian points representing the immersed filament is 50. The parameters used here are $\beta = 1.5$, $Fr = 0.5$, and $L = 1.0$. To trigger the instability, the filament is initially placed inclined at an angle of 0.1π with respect to the flow direction. Figure 9 shows the vorticity distribution in the wake for $\gamma = 0.0015$. Figure 10 shows the time histories of the y-position of the trailing edge for two different bending rigidities. It is seen that the present results agree well with those from Ref. [11] for both cases. Some discrepancies in phase and amplitude are due to the following two factors. First, although in this work we use the same algorithm as that in Ref. [11] in solving the structure equation, the basic solver for solving the N–S equation is different. Second, in Ref. [11] very small time steps are used (CFL number is only around 0.11) due the stability restriction. In the present method, the stability restriction on time step is much looser, and we use larger time steps (CFL is around 0.5).

3.4 Three-Dimensional Simulation of a Flapping Flag. The 3D simulation of a flapping flag is also performed in this paper.

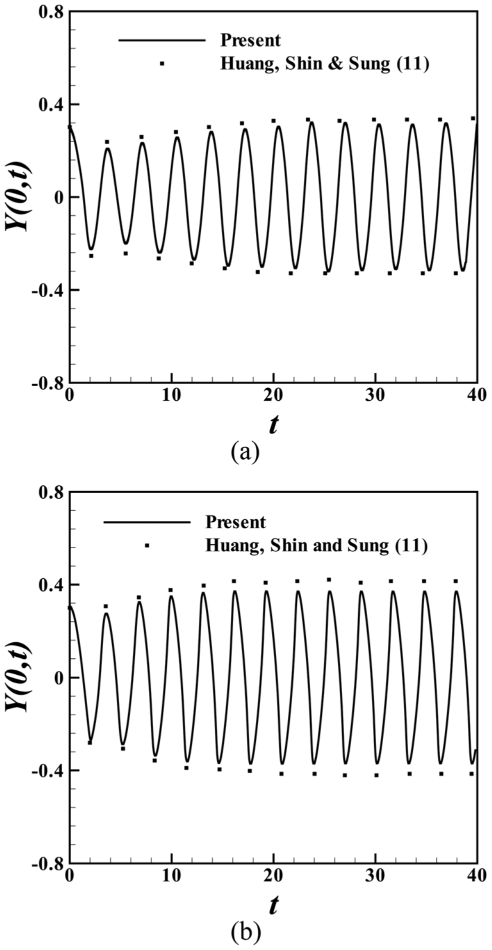

Fig. 10 Time history of *y*-position of the trailing edge: (*a*) $\gamma = 0.0015$ and (*b*) $\gamma = 0.0$

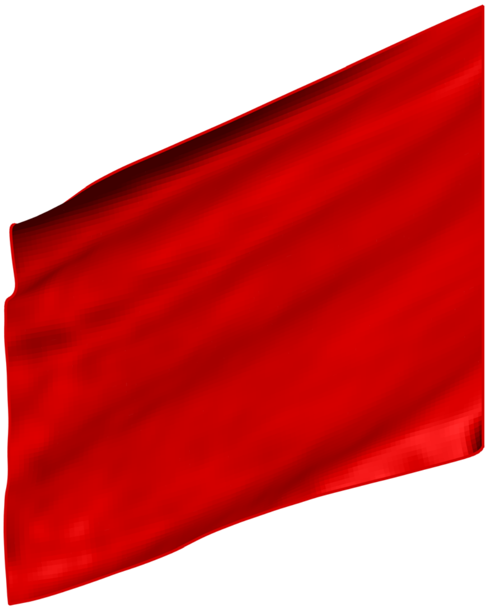

Fig. 11 The instantaneous shape of a flapping flag in the three-dimensional simulation

We use a simply supported condition at the fixed end and free boundary condition at the free end (see Fig. 2 and Eqs. (10)–(13)).

In the simulation of the flapping flag, we use $\sigma_{12} = \sigma_{21} = 10.0$, $\sigma_{11} = \sigma_{22} = 1000.0$, and $\gamma_{12} = \gamma_{21} = \gamma_{11} = \gamma_{22} = 0.0001$ as the

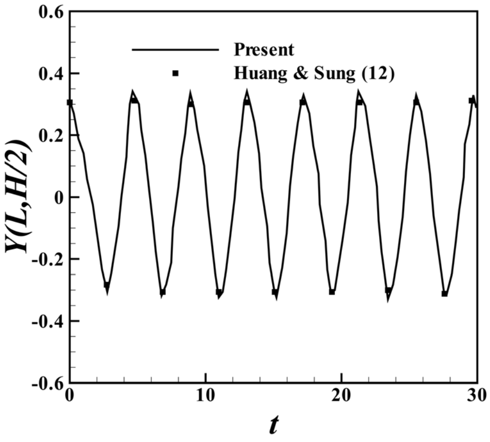

Fig. 12 Time history of the transverse displacement of point A in Fig. 2 for $Fr = 0.0$

control parameters, with a free stream of $\mathrm{Re} = 100$. The computational domain is $8L \times 8L \times 4L$, with the mesh size being $0.02L$ in the vicinity of the flag (a domain of $2L \times 2L \times 2L$). The total number of cells is 2.2×10^6. Other control parameters are $\beta = 1.0$, $Fr = 2.0$, and $L = H = 1.0$. The flag is initially held at an angle of $k = 0.1\pi$ from the XZ plane, as expressed by $\mathbf{X}(s_1, s_2)|_{t=0} = (s_1 \cos k, s_1 \sin k, s_2 - H/2)$.

Figure 11 shows the instantaneous shape of a flapping flag in the three-dimensional simulation. The flag sags down slightly due to the gravitational force. The rolling motion of the upper corner is also seen. These observations are consistent with the report in Ref. [12]. Figure 12 shows the time histories of the transverse displacement of point A in Fig. 2 for $Fr = 0.0$. Both the result of the present study and that of Huang and Sung [12] are plotted in the figure. An excellent agreement between the two results is clearly seen.

4 Conclusions

In this study, an FSI solver is developed for the study of slender structures interacting with fluid. The present solver couples a direct-forcing IB method based on discrete stream function formulation for fluid flow and a staggered-grid finite difference method for the structural motion. Modifications to the original IB method are made to suppress the unphysical spatial oscillations in the force distribution on the surface of the structure. The solver is validated by a series of problems, including flows over stationary circular cylinder and flat plate. FSI simulations performed in this paper include 2D flow over an inextensible filament and 3D flow over a flapping flag. The results obtained in the present study agree well with those in the literature.

Acknowledgment

This work is supported by the Chinese Academy of Sciences under Project Nos. KJCX-SW-L08 and KJCX3-SYW-S01, and the National Natural Science Foundation of China under Project Nos. 10702074, 10872201, 11023001, and 11372331. The authors would like to thank the National Supercomputing Center in Tianjin (NSCC-TJ) for the allocation of computing time.

Nomenclature

$\mathbf{A}$ = implicit operator in discretization
bc = boundary condition vectors in discretization
$\mathbf{C}$ = curl operator
C_d = drag coefficient
C_f = skin friction coefficient
C_l = lift coefficient
C_p = pressure coefficient
$\mathbf{D}$ = divergence operator
D = diameter of the circular cylinder
$\mathbf{f}$ = Eulerian forcing in fluid momentum equation
f = discrete Eulerian force component
$\mathbf{F}$ = Lagrangian forcing in structure equation
$\vec{F}$ = discrete Lagrangian force vector
F = discrete Lagrangian force component
Fr = Froude number
g = magnitude of gravitational acceleration
$\mathbf{g}$ = gravitational acceleration
$\mathbf{G}$ = gradient operator
H = width of the flag
k = initial inclined angle of the filament or flag
L = length of the flat-plat, filament, or flag
O = order of convergence
p = fluid pressure
q = discrete velocity flux
r = explicit term in the discretization of the momentum equation
$\mathbf{R}$ = rotational operator
Re = Reynolds number
s = Lagrangian coordinate
$\tilde{s}$ = discrete stream function
T = tension coefficient of the filament
$\mathbf{u}$ = fluid velocity
u = discrete fluid velocity component
$\vec{U}$ = Lagrangian velocity at the boundary
U = reference velocity
$\mathbf{x}$ = Eulerian coordinate
$\mathbf{X}$ = displacement of the structure
α = angle of attack
β = mass ratio
γ = bending coefficient of the filament or bending and twisting coefficients of the flag
Γ = boundary of the flexible body
δ = regularized δ function
ε = error
θ = angle between radical direction and horizontal direction
ν = kinematic viscosity
σ = stretching and shearing coefficients of the flag
Ω = fluid domain

Subscripts

i, j = index in tensorial material coefficients of the structure or index of node in finite different discretization
k = index of node in finite different discretization
n = index of time step

References

[1] Peskin, C. S., 2003, "The Immersed Boundary Method," Acta Numer., **11**, pp. 479–517.

[2] Mittal, R., and Iaccarino, G., 2005, "Immersed Boundary Methods," Ann. Rev. Fluid Mech., **37**, pp. 239–261.

[3] Balaras, E., and Yang, J., 2005, "Nonboundary Conforming Methods for Large-Eddy Simulations of Biological Flows," ASME J. Fluids Eng., **127**(5), pp. 851–857.

[4] Zhang, N., and Zheng, Z. C., 2007, "An Improved Direct-Forcing Immersed-Boundary Method for Finite Difference Applications," J. Comput. Phys., **221**(1), pp. 250–268.

[5] Narasimhan, M., Dong, H., Mittal, R., and Singh, S. N., 2005, "Optimal Yaw Regulation and Trajectory Control of Biorobotic AUV Using Mechanical Fins Based on CFD Parameterization," ASME J. Fluids Eng., **128**(4), pp. 687–698.

[6] Wang, S., and Zhang, X., 2011, "An Immersed Boundary Method Based on Discrete Stream Function Formulation for Two- and Three-Dimensional Incompressible Flows," J. Comput. Phys., **230**(9), pp. 3479–3499.

[7] Su, S. W., Lai, M. C., and Lin, C. A., 2007, "An Immersed Boundary Technique for Simulating Complex Flows With Rigid Boundary," Comput. Fluids, **36**(2), pp. 313–324.

[8] Uhlmann, M., 2005, "An Immersed Boundary Method With Direct Forcing for the Simulation of Particulate Flows," J. Comput. Phys., **209**(2), pp. 448–476.

[9] Zhu, L., and Peskin, C. S., 2002, "Simulation of a Flapping Flexible Filament in a Flowing Soap Film by the Immersed Boundary Method," J. Comput. Phys., **179**(2), pp. 452–468.

[10] Connell, B. S. H., and Yue, D. K. P., 2007, "Flapping Dynamics of a Flag in a Uniform Stream," J. Fluid Mech., **581**, pp. 33–67.

[11] Huang, W.-X., Shin, S. J., and Sung, H. J., 2007, "Simulation of Flexible Filaments in a Uniform Flow by the Immersed Boundary Method," J. Comput. Phys., **226**(2), pp. 2206–2228.

[12] Huang, W. X., and Sung, H. J., 2010, "Three-Dimensional Simulation of a Flapping Flag in a Uniform Flow," J. Fluid Mech., **653**, pp. 301–336.

[13] Tornberg, A.-K., and Engquist, B., 2004, "Numerical Approximations of Singular Source Terms in Differential Equations," J. Comput. Phys., **200**(2), pp. 462–488.

[14] Linnick, M. N., and Fasel, H. F., 2005, "A High-Order Immersed Interface Method for Simulating Unsteady Incompressible Flows on Irregular Domains," J. Comput. Phys., **204**(1), pp. 157–192.

[15] Taira, K., and Colonius, T., 2007, "The Immersed Boundary Method: A Projection Approach," J. Comput. Phys., **225**(2), pp. 2118–2137.

[16] Majumdar, S., Iaccarino, G., and Durbin, P., 2001, "RANS Solvers With Adaptive Structured Boundary Non-Conforming Grids," Annual Research Briefs, Center for Turbulence Research, Stanford University, pp. 353–466.